



HAL
open science

Indentation Size Effect in Electrodeposited Nickel with Different Grain Size and Crystal Orientation

Petr Haušild, Jaroslav Čech, Miroslav Karlík, Marc Legros, Jiří Nohava,
Benoit Merle

► **To cite this version:**

Petr Haušild, Jaroslav Čech, Miroslav Karlík, Marc Legros, Jiří Nohava, et al.. Indentation Size Effect in Electrodeposited Nickel with Different Grain Size and Crystal Orientation. *Crystals*, 2023, 13 (9), pp.1385. 10.3390/cryst13091385 . hal-04296855

HAL Id: hal-04296855

<https://hal.science/hal-04296855v1>

Submitted on 20 Nov 2023

HAL is a multi-disciplinary open access archive for the deposit and dissemination of scientific research documents, whether they are published or not. The documents may come from teaching and research institutions in France or abroad, or from public or private research centers.

L'archive ouverte pluridisciplinaire **HAL**, est destinée au dépôt et à la diffusion de documents scientifiques de niveau recherche, publiés ou non, émanant des établissements d'enseignement et de recherche français ou étrangers, des laboratoires publics ou privés.

Indentation Size Effect in Electrodeposited Nickel with Different Grain Size and Crystal Orientation

Petr Haušild ^{1*}, Jaroslav Čech ¹, Miroslav Karlík ¹, Marc Legros ², Jiří Nohava ³, Benoit Merle ⁴

¹ Czech Technical University in Prague; Faculty of Nuclear Sciences and Physical Engineering, Prague, Czechia

² CEMES/CNRS, Toulouse, France

³ Anton Paar TriTec; Neuenburg, Switzerland

⁴ University of Kassel; Institute of Materials Engineering, Kassel, Germany

* Correspondence: petr.hausild@ffi.cvut.cz

Abstract: Indentation size effect at shallow indentation depths still remains a challenge as it cannot be correctly described by the Nix-Gao model based on the concept of strain gradient plasticity and geometrically necessary dislocations. The reasons for this discrepancy may be various and multiple microstructural factors may play a role at the nanoscale. In the present paper, the break-down of the Nix-Gao model was explored in electrodeposited nickel with different grain size/shape and crystallographic orientation. Crystallographic orientation has no significant effect on the indentation process at shallow depths if plastic deformation has already developed. On the other hand, decreasing the grain size leads to constrained plastic deformation in the grains below the indenter and to an effective plastic zone expansion. Further grain refinement down to the nanograin material leads to a change in the plastic deformation mechanisms to grain boundary-mediated deformation and a more pronounced breakdown of the Nix-Gao model.

Keywords: nanoindentation; indentation size effect; Nix-Gao model; effective plastic zone

1. Introduction

Indentation size effect (ISE), i.e., size-dependent increase in hardness, occurs in many materials due to unique deformation phenomena operating at small scales [1]. In materials such as ceramics, semiconductor materials, and amorphous materials, the mechanisms responsible for ISE may involve cracking, phase transformations, or non-dislocation-based mechanisms of plasticity [2]. In crystalline plastically deformable materials, ISE generally occurs when the size of the indent approaches the average dislocation spacing, so that the plastic deformation under the indenter is controlled by a limited number of existing defects [2]. This makes it very difficult to compare the values of hardness obtained at different (in particular, small) depths. The model most commonly used to describe ISE is that developed by Nix and Gao [3]. This model is based on the evolution of the density of geometrically necessary dislocations introduced by the change of shape during indenter penetration. In the Nix-Gao model, the dependence of hardness on depth is related to the characteristic length h_0 through the relation:

$$H = H_0 \sqrt{1 + \frac{h_0}{h}} \quad (1)$$

where H_0 is hardness in the limit of infinite depth (i.e., macroscopic hardness).

45 The Nix-Gao model predicts the ISE well for indentations at the micrometre scale,
46 but breaks down (tends to overestimate the hardness) for very shallow indentation
47 depths (see e.g. [4-6]).

48 There are several phenomena that complicate the understanding of ISE at shallow
49 depths (although they cannot fully explain it), such as imperfect indenter geometry or
50 sample surface preparation (see e.g. [4,5]).

51 Swadener et al. [6] proposed that the overestimation of the hardness predicted by
52 the Nix-Gao model for very small indentations may probably result from the strong re-
53 pulsive force between geometrically necessary dislocations which pushes them to spread
54 beyond the hemispherical zone of the contact radius size (leading to the overestimation
55 of the dislocation density at shallow indentation depths). This suggestion was experi-
56 mentally supported e.g. by Ref. [7].

57 Some modifications of the Nix-Gao model have already been proposed based on the
58 maximum allowable geometrically necessary dislocation density [5] and/or an expansion
59 of the storage volume for geometrically necessary dislocations [8-10]. With these models,
60 the Nix-Gao model can be extended to shallow depths. However, the mechanisms re-
61 sponsible for the restriction of maximum allowable dislocation density or the expansion
62 of the effective size of the plastic zone size still remain very partially understood.

63 The present paper aims to explore the break-down of the Nix-Gao model for in-
64 dentation size effect at shallow indentation depths in a model material with different
65 grain sizes and crystal orientation. Particular attention was paid to understanding the
66 role of grain boundaries as insurmountable obstacles for dislocation motion when the
67 grain size is comparable to the indentation depth.

68 2. Material and Methods

69 The material chosen for the study was commercially pure nickel electrolytically
70 plated on the austenitic stainless steel substrate. In pure nickel, plastic deformation is
71 preferentially mediated by dislocation slip, and this material does not show important
72 pile-up around the indents (which would complicate the use of the Oliver-Pharr method
73 [11] on load versus depth of penetration curves).

74 Nickel plating was performed in a standard industrial coater (Galvanic Engineering
75 Service, Ltd., Czechia) using a Nickel sulfamate bath and a current density of 0.01 and 0.1
76 A.cm⁻² to vary the grain size and the preferential crystal growth orientation. The thick-
77 ness of the deposited layer was about 300 μm.

78 After electrolytic plating, the sample surfaces were prepared according to the
79 scheme presented in Fig. 1 (perpendicular and parallel to the growth direction of the Ni
80 layer) and processed by standard metallographic procedure (mechanical grinding and
81 polishing). The final surface finishing consisted of electrolytic polishing (in 5% perchloric
82 acid solution in ethanol, at 40 V) to remove the surface layer affected by cutting, me-
83 chanical grinding, and polishing. One coated sample with [100] fibre texture (see later)
84 was annealed 2 h/1000 °C in air to prepare a coarse-grained reference sample (for the
85 choice of annealing temperature, see e.g. [12,13]). After annealing, the surface was pre-
86 pared and analysed by the same procedure as for the as-deposited state.

87 Metallographic analysis was performed for electropolished samples in a scanning
88 electron microscope (SEM) JEOL IT500HR (JEOL Ltd., Japan) equipped with a Velocity™
89 electron backscatter diffraction (EBSD) camera (EDAX Inc., USA.). The samples were
90 inspected at a 70 ° tilt angle at the positions where nanoindentation tests were performed.
91 The acquired data were evaluated using OIM™ software (EDAX Inc., USA).

92 Transmission electron microscopy (TEM) was performed on the samples in the
93 as-deposited state. The samples for TEM were prepared by cutting the surface layer of
94 the substrate with the Ni deposit using a diamond wafering blade. Subsequently, the
95 surface roughness of the deposit was removed using P1200 SiC paper to obtain a plane.
96 The sample was then turned over and the steel substrate was ground to obtain a 100 μm
97 thick platelet (close to the surface of the deposit). Standard TEM 3 mm discs, cut out us-

ing Gatan Punch, were ground to a thickness of 40 μm . Thin foils were prepared by twin-jet electrolytic polishing ($-32\text{ }^\circ\text{C}$, 20 V) in a Tenupol 5 (Struers, Denmark) device filled with a 6 % HClO_4 solution in methanol. The microstructural investigation was carried out using a JEOL JEM 2000FX (JEOL Ltd., Japan) transmission electron microscope operated at 200 kV.

Nanoindentation measurements were performed on the NHT² Nanoindentation Tester (Anton Paar, Switzerland) with the Berkovich diamond indenter using the instrumented indentation technique [11]. The tip radius of the Berkovich indenter was about 150 nm (the details about the tip radius estimation methods can be found in Refs. [14-16]). The area function was calibrated on fused silica using the standard procedure. The (normal) direction of indentation corresponded to the direction of the Ni growth (orientation top – in axis A3) and perpendicular to the direction of growth (orientation cut – in axis A1). In the top direction, the surface layer of defined thickness was ground off before the indentation so that the measurements were performed at the same location as in the cut direction.

To obtain the mechanical response from different depths, the so-called continuous multicycle (CMC) indentation was used with increasing load, varying the maximum load in each cycle from 0.1 mN to 500 mN. The loading time was 10 s per cycle for CMC, followed by a hold of 5 s at maximum load, and the unloading time was 10 s per cycle. The appropriateness of the method was verified by comparing it with single indentation tests. The results were evaluated according to the ISO 14577 standard. At least 10 CMC indentation tests were performed on each sample.

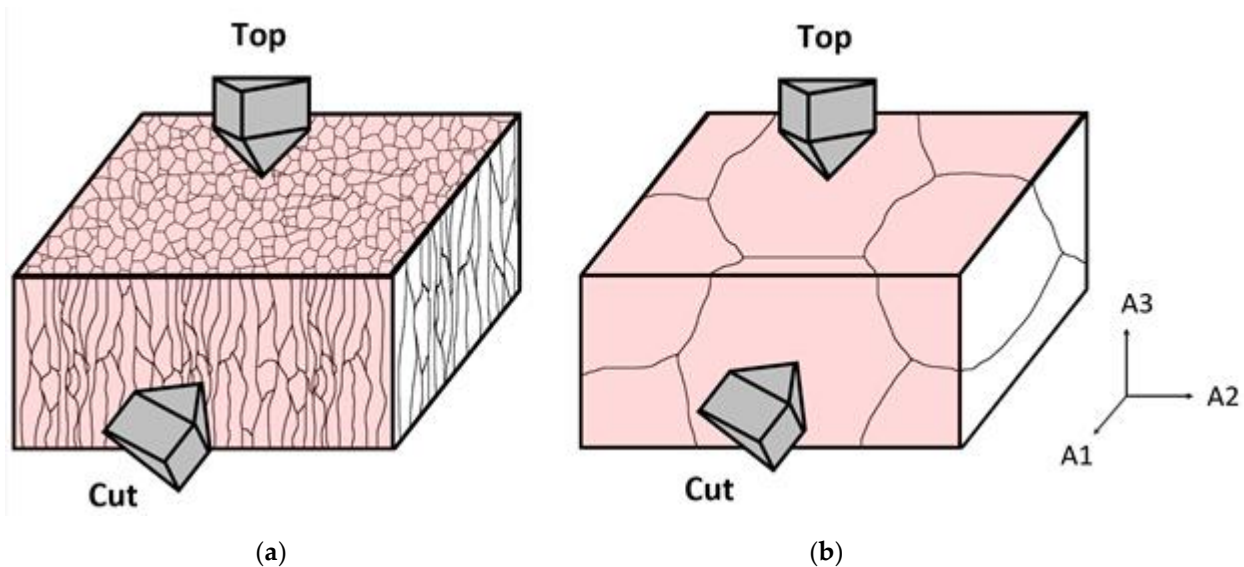


Figure 1. Sample coordinate system and indentation scheme in the electrodeposited layer (a), and after grain coarsening (b). The directions of indentation are denoted Top and Cut.

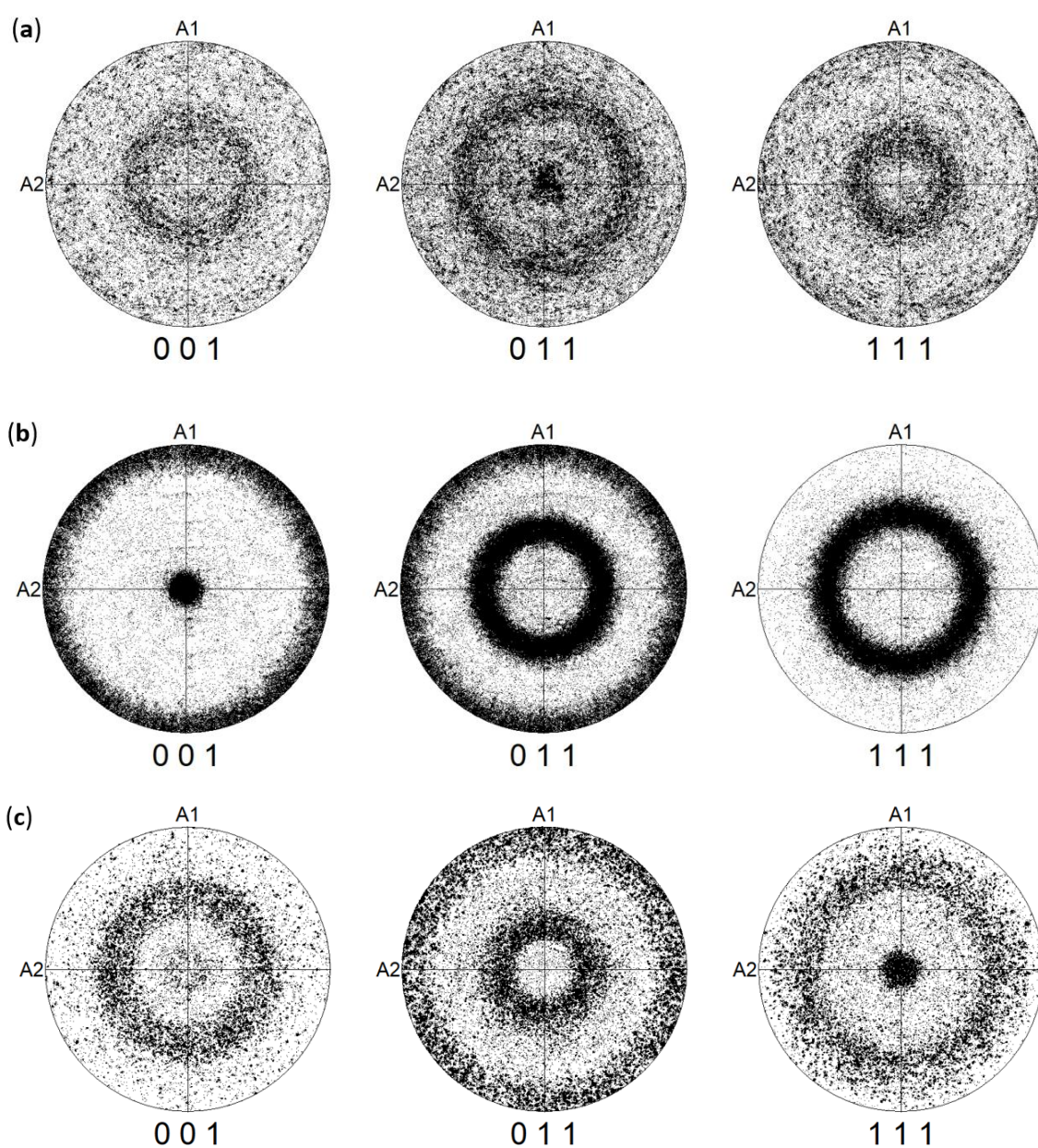


Figure 2. Summary of pole figures in nickel layers obtained by electrodeposition with a current density of 0.01 A.cm^{-2} (a), a current density of 0.1 A.cm^{-2} (b), and after electrodeposition with a current density of 0.1 A.cm^{-2} and annealing $2 \text{ h}/1000 \text{ }^\circ\text{C}$ (c). The direction of growth corresponds to the A3 (normal) axis. Clearly developed [110], [100], and [111] fibres can be observed.

3. Results and Discussion

3.1. Microstructure

The grain size and crystal orientation in the electrodeposited layer varied according to the current density. For the lowest current density (0.01 A.cm^{-2}), the deposition started with an initial very fine-grained thin layer (thickness less than $20 \mu\text{m}$). The grain size was at/below the limit of the EBSD resolution in this layer, so it can be estimated to be less than 100 nm . The crystallographic orientation was "random", however, as stated before, not all orientations of grains could be identified, especially those of the smaller ones. With increasing distance from the substrate, columnar growth with the [110] fibre texture occurred (see Figures 2a and 3).

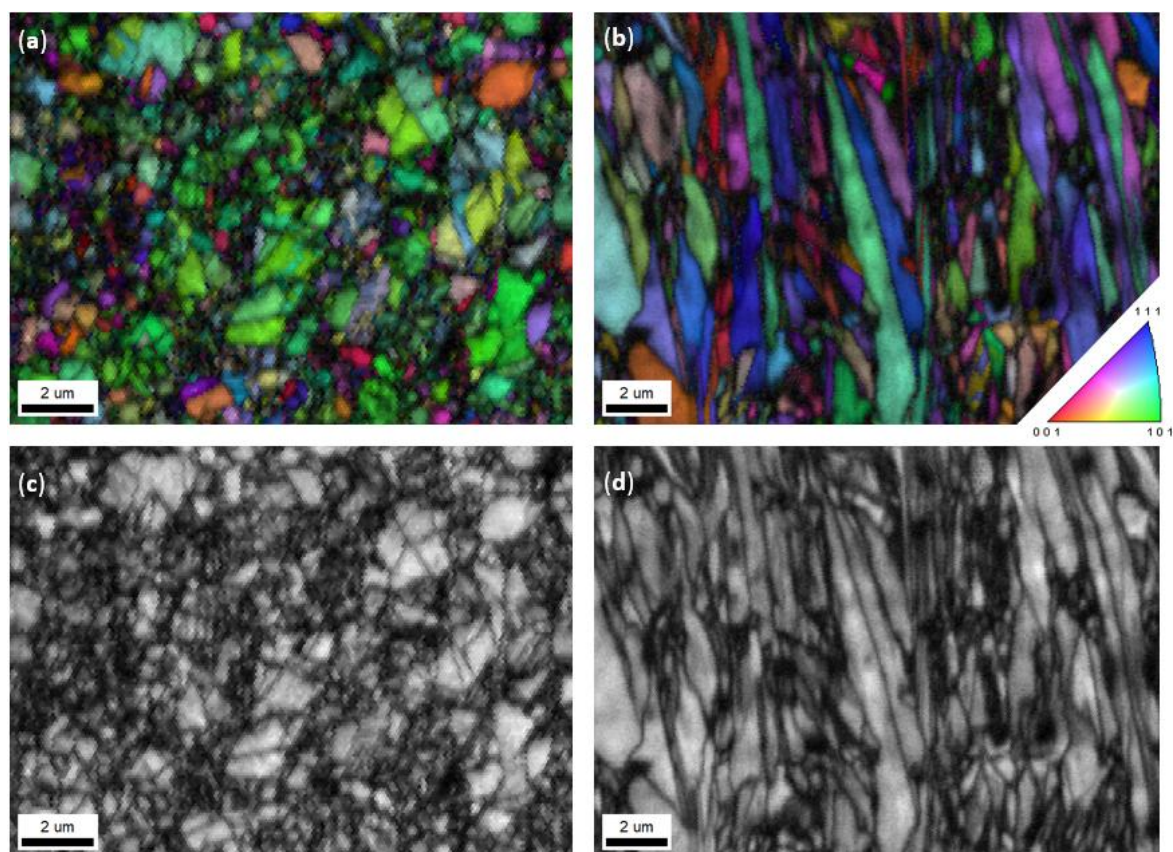


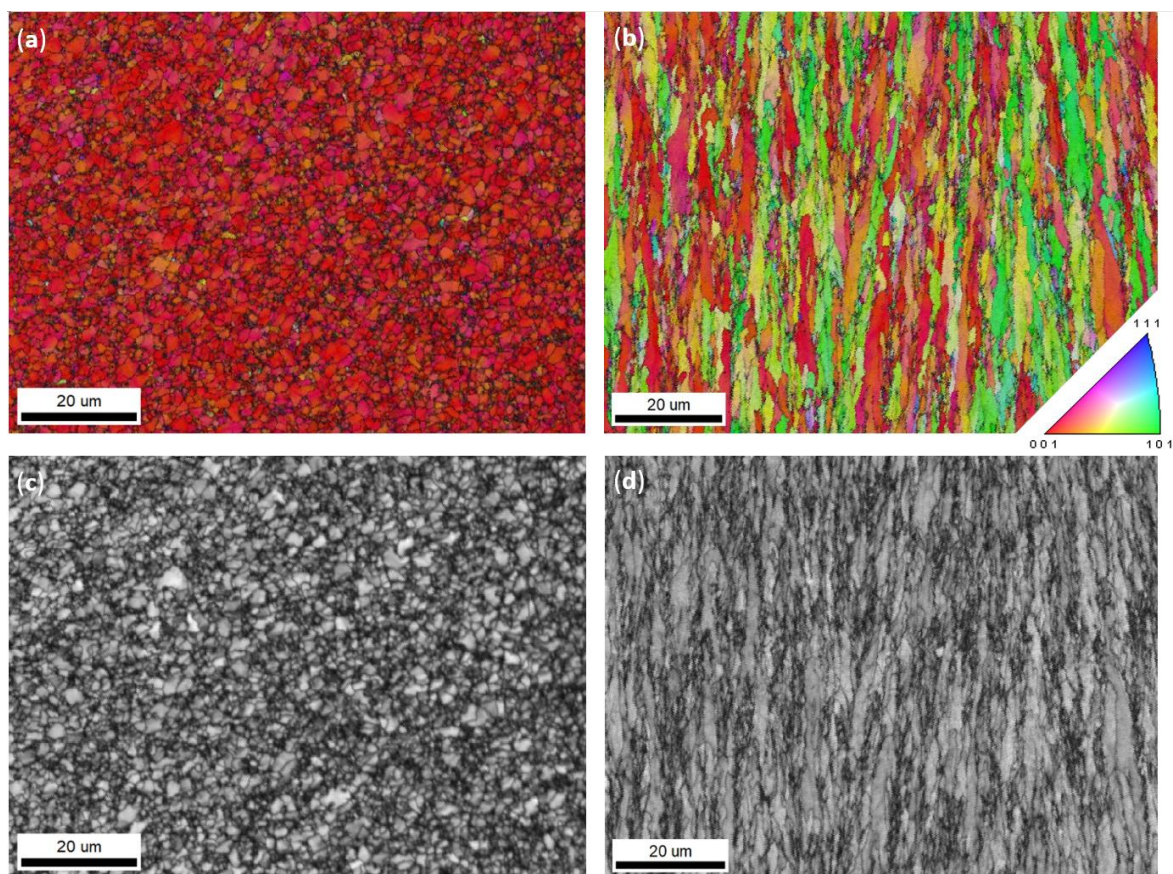
Figure 3. EBSD maps of Ni layer obtained by electrodeposition with a current density of 0.01 A.cm^{-2} . Image quality maps (visualisation of microstructure) with superimposed inverse pole figures showing the crystallographic orientation on the top (a) and in the cut (b) of the sample. Morphology of grains (depicted using image quality maps) on the top (c), and in the cut (d) in the same position.

The grain sizes ranged from hundreds of nanometres to one or two micrometres perpendicular to the direction of growth and up to approximately ten micrometres in the direction of growth. The average grain/column diameter was evaluated in the cut perpendicular to the direction of growth using EBSD to be $0.66 \pm 0.25 \mu\text{m}$.

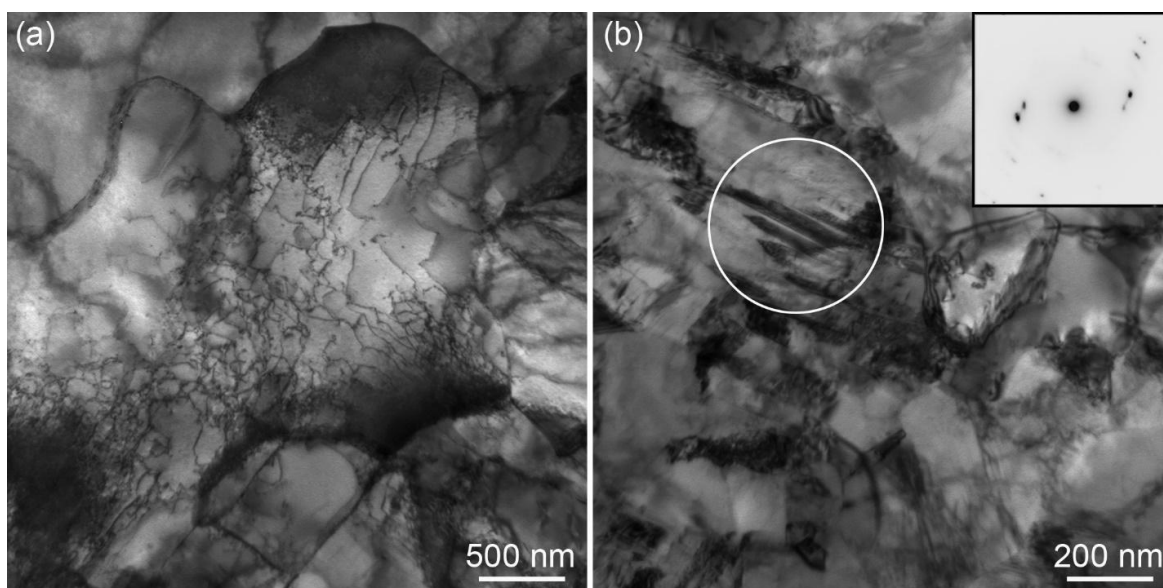
For the current density 0.1 A.cm^{-2} , the columnar growth with the $[100]$ fibre texture stabilised very quickly (Figure 2b). The grain sizes ranged from hundreds of nanometres to a few micrometres perpendicular to the direction of growth and to several tens of micrometres in the direction of growth (Figure 4). The average grain/column diameter in the cut perpendicular to the growth direction was evaluated using EBSD to be $1.17 \pm 0.22 \mu\text{m}$.

These results are in a very good agreement with results of Amblard et al. [17] who found that the grain-oriented growth of Ni coatings changes from $[110]$ to $[100]$ crystal direction, with increasing current density and pointed out that these textures of Ni electrodeposits are attributed to inhibited outgrowth (by hydrogen adsorption) and free-lateral growth, respectively.

TEM observation revealed uneven dislocation substructure (Fig. 5a) and numerous nano twins (Fig. 5b) in both electrodeposited coatings. Some grains contained only a few straight dislocations, in other ones, there were dislocation tangles (Fig. 5a). However, the density of dislocations was generally low.



167
168
169
170
171
172
Figure 4. EBSD maps of Ni layer obtained by electrodeposition with a current density of 0.1 A.cm^{-2} . Image quality maps with superimposed inverse pole figures showing the crystallographic orientation on the top (a), and in the cut (b) of the sample. Visualization of microstructure (using image quality maps) on the top (c), and in the cut (d) in the same position. To note the columnar growth and a distinctive [100] fibre texture.



173
174
175
176
177
178
Figure 5. Bright-field TEM micrographs of the fine microstructure of the nickel layer electrolytically deposited with a current density of 0.1 A.cm^{-2} : (a) Dislocation substructure, (b) Very small grains and grown-in nano twins (the circle shows the size and position of the selective area aperture, the diffraction pattern with twin double diffraction spots is in the inset).

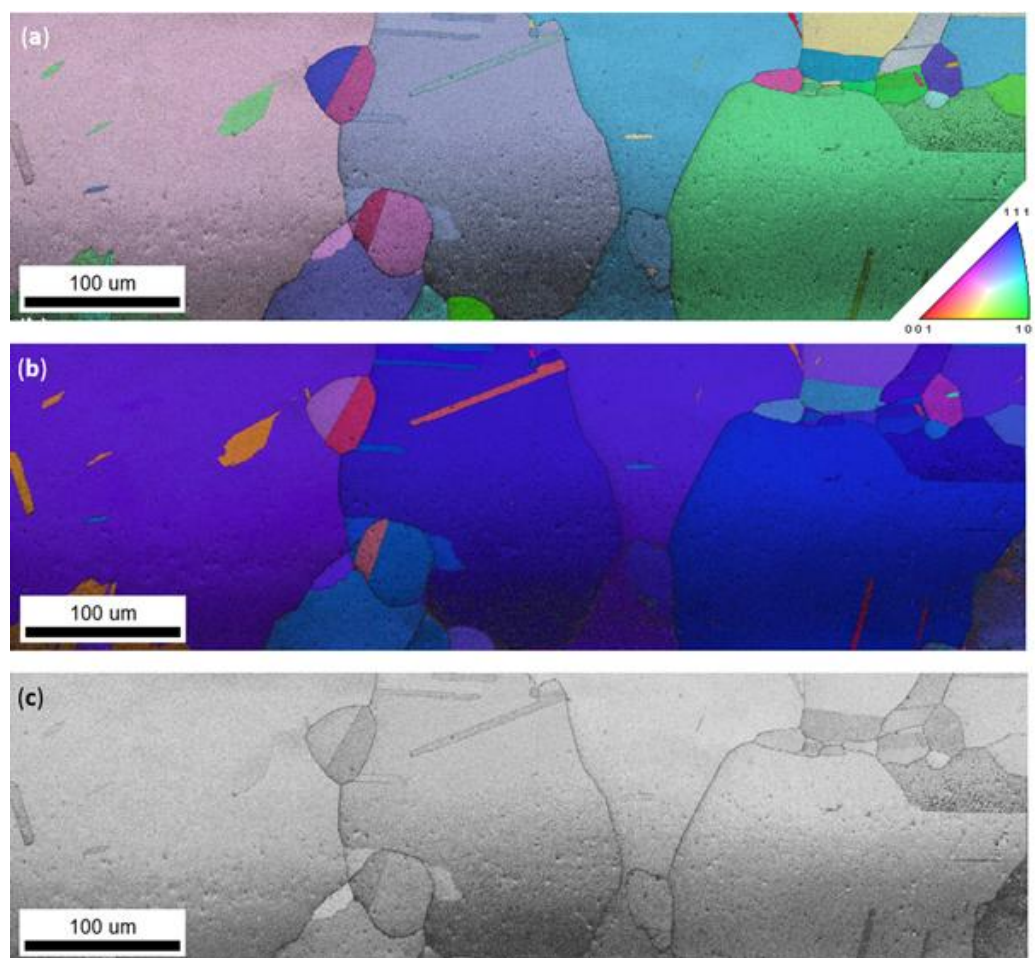


Figure 6. EBSD maps showing the microstructure in the Ni layer after annealing 2 h/1000 °C. Image quality maps with superimposed inverse pole figure showing distribution of the crystallographic orientation in the cut direction – in axis A1 (a), and in the direction perpendicular to the surface – in axis A3 (b) – clear [111] fibre texture in the top orientation can be seen. Image quality map showing the coarse-grained microstructure (c).

The sample coated with a current density of 0.1 A.cm⁻² was annealed to prepare a coarse-grained reference sample. After annealing, the grain sizes varied from tens to hundreds of micrometres (some grains grew through the whole thickness of the Ni layer – see Figure 6). The grain size was substantially higher than the size of the indents, so this sample can be considered as a reference (single crystalline). Annealing led to the development of a [111] fibre texture (Figures 2c and 6b).

With respect to these results, the samples will hereafter be referred to as Ni 111 (annealed) cut/top, Ni 100 cut/top (for layer deposited with the current density of 0.1 A.cm⁻²), Ni 110 cut/top (for layer deposited with the current density of 0.01 A.cm⁻²) and Ni fine grained random (for layer deposited with the current density of 0.01 A.cm⁻² close to the substrate).

3.2. Nanoindentation

The methodology was first verified by comparing the results of the CMC tests with the results of the single-load indentation tests performed (either at a constant load rate or at a constant strain rate) to different depths. No effect of strain rate, creep during the hold period, or cyclic loading-unloading was observed (as expected); the results of the CMC tests and the single indentations were in very good agreement, confirming the validity of the CMC method.

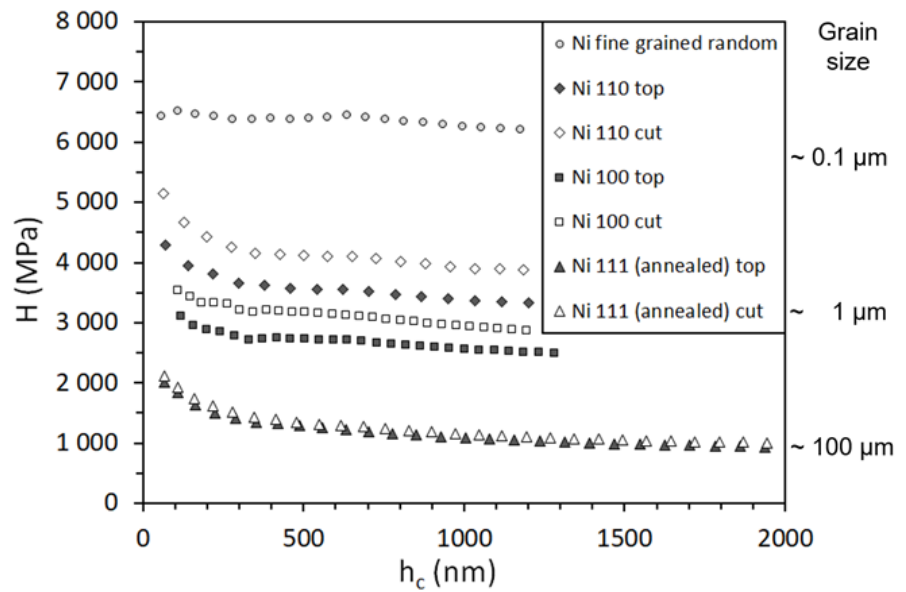


Figure 7. Hardness as a function of contact depth for Ni electrodeposited layers with different grain size and crystallographic orientation.

The evolution of hardness with indentation depth is shown for all characterised samples in Figure 7. Except for the fine-grained, all samples present a significant ISE. In the fine-grained sample, the increase in hardness with decreasing indentation depth is not as pronounced. The hardness increases over all depths with decreasing grain size of the samples. Indeed, the differences in macroscopic hardness (H_0) as well as hardness profile cannot be attributed to crystallographic orientation, as the lowest values were obtained in the annealed sample with the [111] fibre texture. The [111] crystal direction is known to be the hardest in Nickel; however, the triaxial stress field under the indenter makes the effect of crystallographic orientation on hardness negligible (see e.g. [18,19]). In this case, the lower hardness can certainly be attributed to a larger grain size and a lower dislocation density after annealing.

The hardness measured on the cut is systematically higher than the hardness measured in the top direction, although for annealed (coarse-grained) samples this difference is very small. This increase is therefore probably due to the columnar shape of the grains, which creates a shorter free path for dislocation movement in the cut direction.

The depth dependence of the hardness in the form of normalised H^2 vs. $1/h$ plots is shown in Figure 8. The Nix–Gao model (dashed lines) according to Equation (1) fits the data well for depths higher than around $1 \mu\text{m}$ then it deviates. It is also worth noting that after normalisation, the samples with columnar grain structure show very similar curves regardless of the texture fibre ([100] or [110]) or the indentation direction (top or cut).

On the other hand, the annealed sample, with its coarse grains and lower dislocation density, has a substantially lower hardness H_0 and therefore shows distinctly different curves, although very similar in the top or cut indentation directions. Similarly, the fine-grained sample shows a distinctly different curve as it has a substantially higher hardness H_0 .

To explore this deviation in more detail, we analysed the hardness values at shallow indentation depths using the model considering the limitation of the increase in dislocation density due to the spread-out of geometrically necessary dislocations [10].

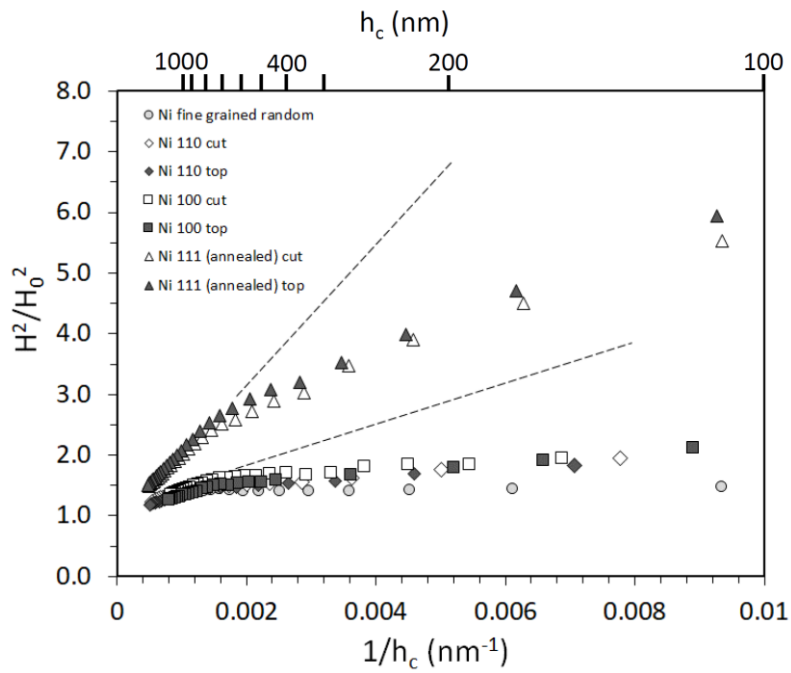


Figure 8. Normalised Nix-Gao plot (H^2 vs. $1/h$) showing the deviation from the Nix-Gao model (dashed lines) fitted for greater depths

The modification of the Nix-Gao model developed in previous research consists in the hardness dependence on penetration depth which can be expressed as:

$$H = H_0 \sqrt{1 + \frac{h_0}{h} \left(1 - e^{-\frac{h^n}{h_1^n}}\right)} \quad (2)$$

where characteristic depth h_1 and shape exponent n are fitting parameters.

This equation can be rewritten in the following form:

$$H = H_0 \sqrt{1 + \frac{h_0}{h} \left(\frac{R_0}{R}\right)^3} \quad (3)$$

where the inverted value of the term in brackets, (R/R_0) , corresponds to the ratio of effective plastic zone expansion and can be obtained for shallow penetration depth as:

$$\frac{R_0}{R}(h) = \sqrt[3]{\left(\frac{H^2}{H_0^2} - 1\right) \frac{h}{h_0}} \quad (4)$$

The ratio of effective plastic zone expansion is shown in Figure 9. It can be seen that the deviation from the Nix-Gao model becomes larger with decreasing grain size. It is also evident that the deviation from the Nix-Gao model starts earlier with decreasing grain size. This trend is apparent from the identified parameters of the modified Nix-Gao model (Table 1).

In the annealed (coarse-grained) sample, the shape exponent n is around 0.7, which is a value comparable with values obtained for pure metals in previous research [10]. In the same way, the parameter h_1 is substantially smaller than the characteristic length h_0 from the Nix-Gao model. The deviation from the Nix-Gao model can therefore be attributed to the spread-out of geometrically necessary dislocations as the result of the strong repulsive force between them in the constrained volume under the indenter as originally proposed by Swadener et al. [6].

258

259

Table 1. Parameters of the modified Nix-Gao model identified on samples with different grain size.

	D (nm)	H ₀ (MPa)	h ₀ (nm)	h ₁ (nm)	n
Ni 111 (annealed) top	~ 10 ⁵	752	1077	37	0.68
Ni 111 (annealed) cut		818	990	37	0.68
Ni 100 top	~ 10 ³	2205	356	85	0.78
Ni 100 cut		2461	427	145	0.73
Ni 110 top	~ 500	2922	368	128	0.80
Ni 110 cut		3343	436	110	0.75
Ni fine grained random	~ 100	5363	408	2260	1.20

260

261

262

263

264

265

266

267

268

269

270

271

272

273

274

275

276

277

278

279

280

281

282

283

284

285

286

287

288

289

290

291

292

293

294

295

Generally, the most important factor that affects the deviation of the measured hardness from the values predicted by the Nix-Gao model is the lattice friction stress [10]. In the coarse-grained sample, the plastic deformation is realised for both the top and the cut orientations by the same slip systems (with the same lattice friction stress) and cannot be substantially affected by distant grain boundaries.

In samples with columnar grains, the shape exponent n is still in the range 0.7-0.8, but the identified parameters h_1 start to approach the characteristic length h_0 . No effect can be expected from the back-stress induced by existing (statistically stored) dislocations, as the density of dislocations after electrodeposition was very low. In this case, the increase in the effective plastic zone size is probably a consequence of the constraint on the free path for dislocation movement by grain boundaries, resulting in a limited dislocation density inside the grains and a transfer of plastic deformation to adjacent plastically undeformed grains. The spreading of the plastic zone out of the indented single grains caused by the pile-up of dislocations was proposed as a direct evidence of the activation of new dislocation sources in the neighbouring grains in Refs [20,21].

For the fine-grained sample, the situation is completely different. The deviation from the Nix-Gao model starts earlier (for the depths higher than 1 μm) and is very pronounced. The identified shape parameter n is greater than 1, and the parameter h_1 is greater than the characteristic length h_0 . In other words, although the hardness is very high and for greater indentation depths, it more or less follows the Nix-Gao models, the ISE is very limited at shallow indentation depths. For very shallow indentation depths (< 50 nm) and ultrafine grained or nanocrystalline materials, even inverse ISE has been observed in the literature (see e.g. Refs. [20,22,23]). However, depths lower than 50 nm were not explored in our paper as the results would inevitably be affected by the change in indenter shape (from pyramidal to rounded) and the onset of plasticity (before first massive pop-in).

It is therefore hypothesised that the mechanisms of plastic deformation are different from the previous cases and involve a predominant role of grain boundary-controlled mechanisms such as boundary sliding, grain rotation, and/or grain boundary migration [24,25]. The change in the deformation mechanism from dislocation-controlled deformation to grain boundary-mediated deformation can make the use of the concept of an extended (effective) plastic zone problematic, and the (modified) Nix-Gao model originally based on geometrically necessary dislocations should be used with care in this case.

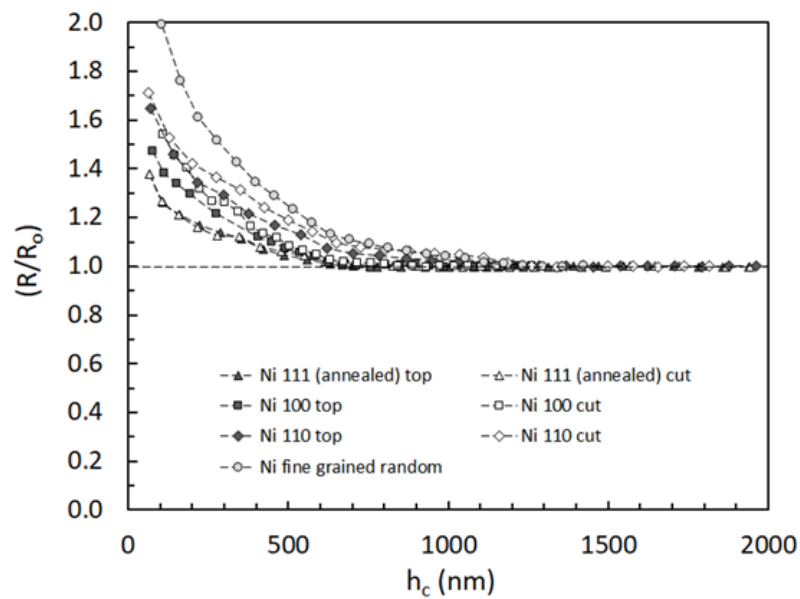


Figure 9. Increase in effective plastic zone size for shallow indentation depths. To note that the deviation from the Nix-Gao model ($R/R_0=1$) becomes larger with decreasing grain size.

4. Conclusions

The break-down of the Nix-Gao model for indentation size effect at shallow indentation depths was explored in model material with different grain sizes and crystal orientation.

It was confirmed that crystallographic orientation plays a minor role even in deviations from the Nix-Gao model at shallow depths if plastic deformation is already developed under the indenter.

In contrast, decreasing grain size leads to constrained plastic deformation in the grains below the indenter and a progressive deviation from the Nix-Gao model. The evolution of the identified parameters of the modified Nix-Gao model is consistent with the assumed expansion of the plastic zone and the activation of new dislocation sources in adjacent grains.

Further grain refinement down to the nanograin material leads to a probable change in the plastic deformation mechanisms from dislocation-based to grain boundary-mediated deformation and results in an earlier and more pronounced breakdown of the Nix-Gao model for the indentation size effect.

Author Contributions: Conceptualization, P.H. and B.M.; methodology, P.H. and J.Č.; investigation, P.H., J.Č., J.N. and M.K.; writing—original draft preparation, P.H., J.Č., J.N. and M.K.; writing—review and editing, M.L. and B.M. All authors have read and agreed to the published version of the manuscript.

Funding: This research was funded by OP RDE No.CZ.02.1.01/0.0/0.0/16_019/0000778, Centre of Advanced Applied Sciences (CAAS) and COST Action CA21121, European Network for the Mechanics of Matter at the Nano-Scale (MecaNano).

Data Availability Statement: Raw data are available upon reasonable request.

Conflicts of Interest: The authors declare no conflict of interest. The funders had no role in the design of the study; in the collection, analyses, or interpretation of data; in the writing of the manuscript; or in the decision to publish the results.

References

1. Manika, I.; Maniks, J. Size effects in micro- and nanoscale indentation. *Acta Mater.* **2006**, *54*, 2049-2056. <https://doi.org/10.1016/j.actamat.2005.12.031>
2. Pharr, G.M.; Herbert, E.G.; Gao, Y. The indentation size effect: A critical examination of experimental observations and mechanistic interpretations. *Annu. Rev. Mater. Res.* **2010**, *40*, 271–292. <https://doi.org/10.1146/annurev-matsci-070909-104456>
3. Nix, W.D.; Gao, H. Indentation size effects in crystalline materials: A law for strain gradient plasticity. *J. Mech. Phys. Solids.* **1998**, *46*, 411-425. [https://doi.org/10.1016/S0022-5096\(97\)00086-0](https://doi.org/10.1016/S0022-5096(97)00086-0)
4. K. Durst, B. Backes, and M. Göken, Indentation size effect in metallic materials: Correcting for the size of the plastic zone. *Scr. Mater.* **52** (2005), pp. 1093-1097. <https://doi.org/10.1016/j.scriptamat.2005.02.009>
5. Huang, Y.; Zhang, F.; Hwang, K.C.; Nix, W.D.; Pharr, G.M.; Feng, G. A model of size effects in nano-indentation, *J. Mech. Phys. Solids* **2006**, *54*, 1668-1686. <https://doi.org/10.1016/j.jmps.2006.02.002>
6. Swadener, J.G.; George, E.P.; Pharr, G.M. The correlation of the indentation size effect measured with indenters of various shapes, *J. Mech. Phys. Solids* **2002**, *50*, 681-694. [https://doi.org/10.1016/S0022-5096\(01\)00103-X](https://doi.org/10.1016/S0022-5096(01)00103-X)
7. Rester, M.; Motz, C.; Pippan R. Where are the geometrically necessary dislocations accommodating small imprints? *J. Mater. Res.* **2009**, *24*, 647-651. <https://doi.org/10.1557/jmr.2009.0131>
8. Durst, K.; Backes, B.; Franke, O.; Göken, M. Indentation size effect in metallic materials: Modeling strength from pop-in to macroscopic hardness using geometrically necessary dislocations. *Acta Mater.* **2006**, *54*, 2547-2555. <https://doi.org/10.1016/j.actamat.2006.01.036>
9. Feng, G.; Nix, W.D. Indentation size effect in MgO. *Scr. Mater.* **2004**, *51*, 599-603. <https://doi.org/10.1016/j.scriptamat.2004.05.034>
10. Haušild, P. On the breakdown of the Nix-Gao model for indentation size effect, *Phil. Mag.* **2021**, *101*, 420-434. <https://doi.org/10.1080/14786435.2020.1841916>
11. Oliver, W.C.; Pharr, G.M. An improved technique for determining hardness and elastic modulus using load and displacement sensing indentation experiments. *J. Mater. Res.* **1992**, *7*, 1564-1583. <https://doi.org/10.1557/JMR.1992.1564>
12. Randle, V.; Rios, P.R.; Hu, Y. Grain growth and twinning in nickel, *Scr. Mater.* **2008**, *58*, 130-133. <https://doi.org/10.1016/j.scriptamat.2007.09.016>
13. De Reca, N.W.; Pampillo, C. A. Grain boundary diffusivity via bulk diffusion measurements during grain growth. *Scr. Metall.* **1975**, *9*, 1355–1361. [https://doi.org/10.1016/0036-9748\(75\)90454-8](https://doi.org/10.1016/0036-9748(75)90454-8)
14. Čech, J.; Haušild, P.; Materna, A.; Kovářik, O. Examination of Berkovich indenter tip bluntness. *Mater. Des.* **2016**, *109*, 347-353. <https://doi.org/10.1016/j.matdes.2016.07.033>
15. Chicot, D.; Yetna N'Jock, M.; Puchi-Cabrera, E.S.; Iost, A.; Staia, M.H.; Louis, G.; Bouscarrat, G.; Aumaitre, R. A contact area function for Berkovich nanoindentation: Application to hardness determination of a TiHfCN thin film. *Thin Solid Films* **2014**, *558*, 259-266. <http://doi.org/10.1016/j.tsf.2014.02.044>
16. Nohava, J.; Čech, J.; Havlíček, M.; Consiglio, R. Indenter wear study and proposal of a simple method for evaluation of indenter blunting. *J. Mater. Res.* **2021**, *36*, 4449-4459. <https://doi.org/10.1557/s43578-021-00401-4>
17. Amblard, J.; Froment, M.; Maurin, G.; Spyrellis, N.; Trevisan-Souteyrand, E. Nickel electrocrystallization-from nucleation to textures. *Electrochim. Acta* **1983**, *28*, 909-915. [https://doi.org/10.1016/0013-4686\(83\)85166-4](https://doi.org/10.1016/0013-4686(83)85166-4)
18. Stinville, J.C.; Tromas, C.; Villechaise, P.; Templier, C. Anisotropy changes in hardness and indentation modulus induced by plasma nitriding of 316L polycrystalline stainless steel, *Scr. Mater.* **2011**, *64*, 37-40. <https://doi.org/10.1016/j.scriptamat.2010.08.058>
19. Haušild, P.; Materna, A.; Nohava, J. Characterization of anisotropy in hardness and indentation modulus by nanoindentation. *Metallogr. Microstruct. Anal.* **2014**, *3*, 5-10. <https://doi.org/10.1007/s13632-013-0110-8>
20. Yang, B.; Vehoff, H. Dependence of nanohardness upon indentation size and grain size – A local examination of the interaction between dislocations and grain boundaries, *Acta Mater.* **2007**, *55*, 849-856. <https://doi.org/10.1016/j.actamat.2006.09.004>
21. Jung, B.B.; Lee, H.K.; Park H.C. Effect of grain size on the indentation hardness for polycrystalline materials by the modified strain gradient theory. *Int. J. Solids Struct.* **2013**, *50*, 2719-2724. <https://doi.org/10.1016/j.ijsolstr.2013.05.002>
22. Jang, D.; Greer, J.R. Size-induced weakening and grain boundary-assisted deformation in 60 nm grained Ni nanopillars. *Scripta Mater.* **2011**, *64*, 77-80. <https://doi.org/10.1016/j.scriptamat.2010.09.010>
23. Ma, X.K.; Chen, Z.; Lu, W.J.; Xiao, L. Continuous multi-cycle nanoindentation behavior of a gradient nanostructured metastable β titanium alloy fabricated by rotationally accelerated shot peening. *Mater. Sci. Eng. A* **2021**, *799*, 140370. <https://doi.org/10.1016/j.msea.2020.140370>
24. Yu, Q.; Legros, M.; Minor, A.M. In situ TEM nanomechanics. *MRS Bulletin* **2015**, *40*, 62–70. <https://doi.org/10.1557/mrs.2014.306>
25. Mompioni, F.; Legros, M. Quantitative grain growth and rotation probed by in-situ TEM straining and orientation mapping in small grained Al thin films. *Scripta Mater.* **2015**, *99*, 5-8, <https://doi.org/10.1016/j.scriptamat.2014.11.004>

Disclaimer/Publisher's Note: The statements, opinions and data contained in all publications are solely those of the individual author(s) and contributor(s) and not of MDPI and/or the editor(s). MDPI and/or the editor(s) disclaim responsibility for any injury to people or property resulting from any ideas, methods, instructions or products referred to in the content.